

Research Article

Highly efficient single-crystalline $\text{NaNb}_{1-x}\text{Ta}_x\text{O}_3$ ($x = 0.125$) wires: The synergistic effect of tantalum-doping and morphology on photocatalytic hydrogen evolution

Qianqian Liu^{a,*}, Quan Zhang^b, Lu Zhang^b, Wei-Lin Dai^{b,*}

^a School of Chemistry, Biology and Materials Engineering, Suzhou University of Science and Technology, Suzhou 215009, China

^b Department of Chemistry and Shanghai Key Laboratory of Molecular Catalysis and Innovative Materials, Fudan University, Shanghai 200433, China



ARTICLE INFO

Article history:

Received 27 November 2019

Received in revised form 24 February 2020

Accepted 3 March 2020

Available online 14 May 2020

Keywords:

$\text{NaNb}_{0.875}\text{Ta}_{0.125}\text{O}_3$ wires

Single crystal

Ta-doping effect

Photocatalytic H_2 production

Mechanism

ABSTRACT

For the first time in this work, we manage to synthesize single-crystalline $\text{NaNb}_{0.875}\text{Ta}_{0.125}\text{O}_3$ wires by combining the advantages of one-dimensional (1D) nanostructure and heteroatom doping strategy. Careful Ta doping was performed to figure out the correlation between morphological and structural evolution as well as the photocatalytic performance towards H_2 generation. It was found that, the as-prepared $\text{NaNb}_{0.875}\text{Ta}_{0.125}\text{O}_3$ wires presented a highest and stable photocatalytic performance, which was appropriately 41 and 2 folds higher than that of bare NaTaO_3 and NaNbO_3 . The optical activity was mainly ascribed to the synergistic effect between appropriate Ta doping and perfect 1D wire-like morphology, which resulted in fewer defects, improved charge transfer efficiency and higher reduction capability of electrons. On the other hand, a possible photocatalytic mechanism of photocatalytic H_2 production was proposed in detail. This work creates a new perspective into designing multi-component materials and understanding the mechanism of H_2 evolution, which offers new opportunities for solar-energy conversion.

© 2020 Published by Elsevier Ltd on behalf of The editorial office of Journal of Materials Science & Technology.

1. Introduction

Considering the severe situation on energy crises and environmental pollution, the hydrogen evolution by photocatalytic technology has exhibited great promise because of its environmental friendliness and possibility to replace fossil fuels [1–4]. Various types of photocatalysts have been explored to produce hydrogen, such as TiO_2 [5–7], $g\text{-C}_3\text{N}_4$ [8–10] and sulfides [11,12]. Among which niobates and tantalates show potential due to their particular layered structure and excellent chemical stability [13,14]. Some of niobates and tantalates, including NaNbO_3 [15], SrTa_2O_6 [16], SnNb_2O_6 [17] and MgTa_2O_6 [18,19], have proven to be efficient semiconductor photocatalysts and exhibited superb performance as well.

Perovskite NaNbO_3 and NaTaO_3 , as one of typical niobates and tantalates, have been comprehensively researched recently because of their unique advantages, including easy construction

of controllable morphology and special perovskite-type structure (ABX_3), etc. [20,21]. However, some problems, such as low quantum efficiency and wide band gap (3.0–4.7 eV), still exist and greatly hinder their large-scale application [22]. To deal with the above-mentioned issues, heteroatom doping at the A, B and/or X sites is regarded as an effective strategy [23]. Because the composition and symmetry structure of these materials may be changed through this method, which greatly determined their band structure and photocatalytic properties [24].

To date, co-doping at the A, B and/or O sites of niobates and tantalates (such as $\text{A}_2\text{BNb}_2\text{O}_7$, $\text{A}_2\text{BTa}_2\text{O}_7$, $\text{AB}_2\text{Nb}_3\text{O}_{10}$) (where A = Li, Na, K and B = Ca, Sr, Ba) have been widely used in ferroelectric and dielectric domains [25–27]. However, there are still limited studies on the photocatalytic application. Jana et al. synthesized $\text{NaNb}_x\text{Ta}_{1-x}\text{O}_3$ powders by substituting Ta^{5+} cations with isovalent Nb^{5+} cations and achieved great improvement of photocatalytic activity compared with pure NaTaO_3 . However, the products were always irregular and rough, which dramatically influenced their performance [28]. Besides, heteroatom introduction always resulted in poor crystallinity and increased defects, leading to the recombination of electron-hole pairs [29]. Therefore,

* Corresponding authors.

E-mail addresses: liuqianqian@usts.edu.cn (Q. Liu), wldai@fudan.edu.cn (W.-L. Dai).

controlling the morphology and crystallinity in the process of heteroatom doping are still of great challenge and worth investigating.

Generally, the properties of semiconductor materials, including NaNbO_3 and NaTaO_3 , have a strong morphology dependence [30]. Because different morphologies significantly influence the optical capture ability, active site number and accessibility to reactive actives [31]. Especially, 1D nanostructure, including nanotubes, nanorods and nanowires, have gained much attention because of the advantages such as high aspect ratio, quantum refinement effects and more reactive activities [32,33]. By virtue of these advantages, combining the 1D nanostructure and heteroatom doping strategy to improve the photoactivity of photocatalysts are still greatly attractive.

In this work, 1D single-crystalline $\text{NaNb}_{0.875}\text{Ta}_{0.125}\text{O}_3$ wires were successfully synthesized through a facile hydrothermal strategy for the first time. Careful Ta doping was performed to control the morphological and structural evolution during the reaction process. The photocatalytic H_2 production of different samples was comparatively studied. It was found that the photocatalytic activity of $\text{NaNb}_{0.875}\text{Ta}_{0.125}\text{O}_3$ wires was greatly improved by contrast with pure NaNbO_3 and NaTaO_3 . In addition, a possible mechanism of photocatalytic H_2 production was explored in detail.

2. Experimental

2.1. Materials

All the chemicals, including niobium oxide (Nb_2O_5), tantalum oxide (Ta_2O_5) and sodium hydroxide (NaOH) were purchased from Sinopharm Chemical Reagent Co., Ltd., China, and no further purification was performed.

2.2. Preparation

For the preparation of $\text{NaNb}_{1-x}\text{Ta}_x\text{O}_3$, a series of mixtures of Nb_2O_5 and Ta_2O_5 were added into 10 M NaOH solution under constant stirring for 60 min. The molar ratio of Nb/Ta was 9:1, 7:1, 3:1, 1:1 and 1:3, respectively. After that, the above suspensions were transferred to a 100 mL Teflon-lined stainless steel autoclave and heated at 180 °C for 2 h to produce white solids. Next, the precipitates were washed with DI water and anhydrous ethanol, respectively, and then dried at 100 °C overnight. Finally, the resultant samples were annealing at 500 °C for 12 h. The corresponding products were denoted as $\text{NaNb}_{0.9}\text{Ta}_{0.1}\text{O}_3$, $\text{NaNb}_{0.875}\text{Ta}_{0.125}\text{O}_3$, $\text{NaNb}_{0.75}\text{Ta}_{0.25}\text{O}_3$, $\text{NaNb}_{0.5}\text{Ta}_{0.5}\text{O}_3$ and $\text{NaNb}_{0.25}\text{Ta}_{0.75}\text{O}_3$, respectively.

The atomic ratios of $\text{NaNb}_{1-x}\text{Ta}_x\text{O}_3$ wires were confirmed by X-ray fluorescence spectrometer measurement (XRF). As shown in Table S1, the atomic ratios of Nb/Ta in $\text{NaNb}_{0.9}\text{Ta}_{0.1}\text{O}_3$, $\text{NaNb}_{0.875}\text{Ta}_{0.125}\text{O}_3$, $\text{NaNb}_{0.75}\text{Ta}_{0.25}\text{O}_3$, $\text{NaNb}_{0.5}\text{Ta}_{0.5}\text{O}_3$ and $\text{NaNb}_{0.25}\text{Ta}_{0.75}\text{O}_3$ were measured to be 8.23, 6.11, 2.85, 1.24 and 0.35, respectively. The result showed that the chemical composition of the samples was close to the theoretical values that designed.

For the synthesis of NaNbO_3 and NaTaO_3 , the procedure was the same as above except pure Nb_2O_5 and Ta_2O_5 were used instead of the mixture.

2.3. Characterization of the catalysts

The powder XRD was carried out on a Bruker D8 advance spectrometer with $\text{CuK}\alpha$ radiation ($\lambda = 0.154$ nm) in a 2θ range from 10° to 90°. The morphology and crystal structure were characterized by scanning electron micrographs (SEM) with a PHILIPS XL 30 microscope operating at accelerating voltage of 20 kV and

JOEL JEM 2010 transmission electron microscope (TEM). The low-temperature EPR spectra were performed on a JES-FA200 ESR spectrometer at 103 K. FT-IR and Laser Raman Spectra were implemented on a Nicolet Avatar-360 FT-IR Spectrometer and Horiba Jobin Yvon XploRA Raman spectrometer. XPS was conducted on an RBD 147 upgraded Perkin Elmer PHI 5000C ESCA system equipped with a dual X-ray source. Ultraviolet visible diffuse reflectance spectra (UV-vis DRS) spectra were obtained on a SHIMADZU UV-2450 instrument with BaSO_4 as a reference. Photoluminescence (PL) spectra were measured on a JASCO FP-6500 type fluorescence system. The photocurrent density measurements were performed on an electrochemical workstation (CHI 760E) equipped with a standard three-electrode system including Ag/AgCl electrode, platinum wire and counter electrode. Irradiation was performed with a 300 W Xe-lamp (Ceaulight, CEL-HXF300) as light source. 0.5 M Na_2SO_4 aqueous solution was used as the electrolyte solution. In the preparation of working electrodes, 3 mg of sample powder was suspended into 1 mL of ethanol and ultrasonically dispersed to obtain a slurry. Then, the slurry was dispersed onto the ITO glass (10 mm x 10 mm) and then dried at 120 °C for 30 min to remove ethanol. Electrochemical impedance spectroscopy (EIS) experiment was carried out on a ZENNIUM electrochemical workstation (Zahner, Germany). EIS was conducted in a frequency range of 200 kHz to 5 MHz for 10 mV in DC potential of open circuit potential (OCP) after a 10 min delay.

2.4. Photocatalytic test

Water-splitting reaction was performed on a vessel equipped with a glass closed gas circulation system which used a 300 W Xe arc lamp (Ceaulight, CEL-HXF300) as light source. In a typical process, 100 mg power was suspended in mixed aqueous solution containing deionized water (80 mL), CH_3OH scavenger (20 mL) and the loading of 0.5 wt% Pt as cocatalyst. Prior to irradiation, the above solution was thoroughly degassed to remove air. The H_2 content was measured by gas chromatograph (TCD, with argon as a carrier gas and a 5 Å molecular sieve column).

3. Results and discussion

3.1. Phase structure and morphology

XRD was employed to investigate the crystal structure of $\text{NaNb}_{1-x}\text{Ta}_x\text{O}_3$. As illustrated in Fig. 1(a), all samples exhibit similar XRD patterns. For pure NaNbO_3 , diffraction peaks at 22.7°, 32.5°, 46.3°, 52.6°, 58.0°, 46.8° and 68.0° can be ascribed to (101), (141), (202), (080), (181), (143) and (371) planes, respectively [34], which is well in line with the four-fold orthorhombic perovskite structure (JCPDS card 33–1270). While NaTaO_3 match well with the two-fold orthorhombic perovskite structure (JCPDS card 74–2478) [35]. With the increase of Ta amount, the patterns of all samples exhibit little alteration and still maintain their high crystallinity, indicating Ta^{5+} successfully incorporates into the lattice of NaNbO_3 crystal and influence the positions of Nb^{5+} due to the same ionic radius of both Nb^{5+} and Ta^{5+} [36]. From the partial magnified images in Fig. 1b, the splitting of peaks around 44° and 50° (2θ) obviously decrease with increasing niobium/tantalum ratio, confirming the phase transformation from NaNbO_3 to NaTaO_3 . What's more, the perovskite-type structure of NaNbO_3 is dominant when Nb:Ta ratio is 3:1 or higher. However, the perovskite-type structure of NaTaO_3 become a dominant one after further increasing the content of Ta.

The morphology of the samples was investigated by SEM, TEM and HRTEM. The SEM image in Fig. S1(a) demonstrates that pure NaNbO_3 is composed by 1D wires structure, which is about 100 nm in diameter and tens of micrometers in length. However,

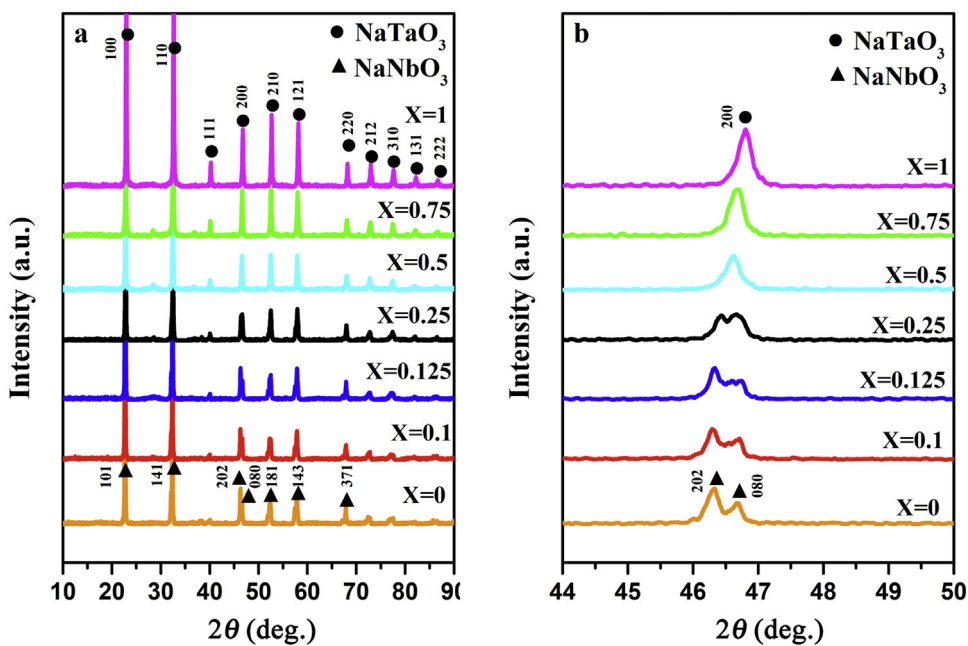


Fig. 1. XRD patterns of $\text{NaNb}_{1-x}\text{Ta}_x\text{O}_3$ samples: (a) the whole patterns; (b) the patterns of certain angle.

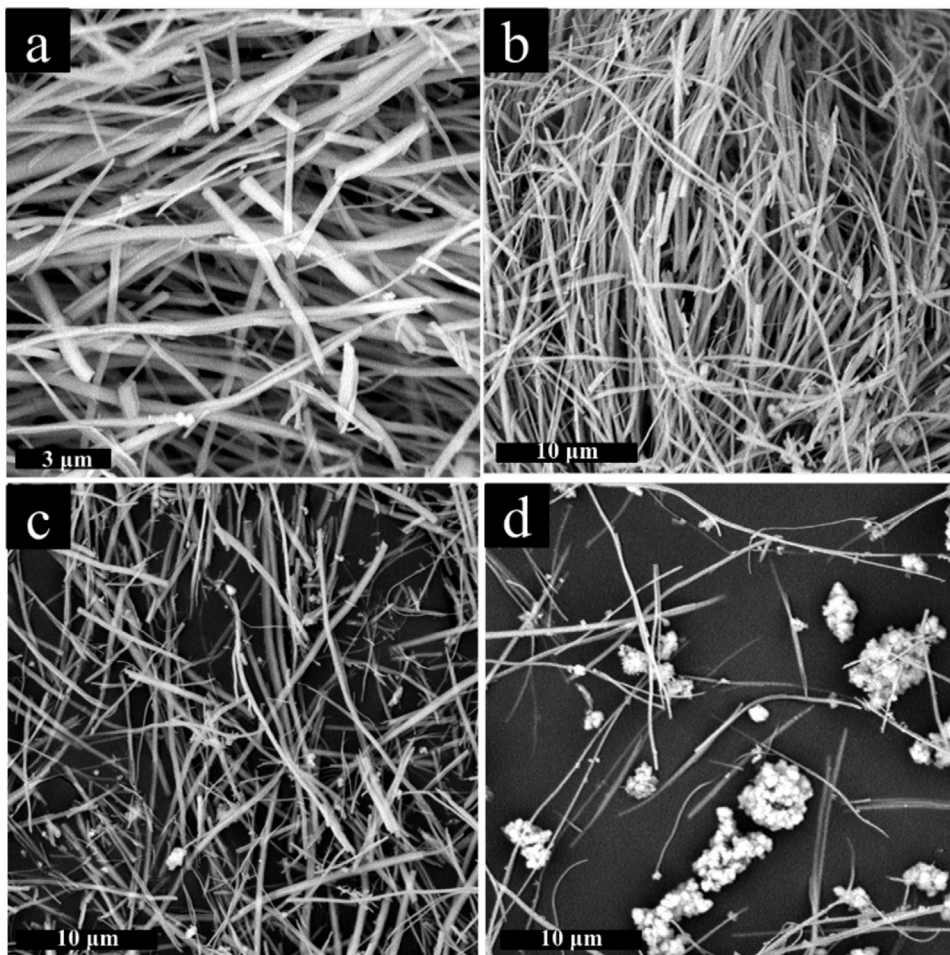


Fig. 2. SEM images of $\text{NaNb}_{0.875}\text{Ta}_{0.125}\text{O}_3$ (a, b), $\text{NaNb}_{0.75}\text{Ta}_{0.25}\text{O}_3$ (c) and $\text{NaNb}_{0.5}\text{Ta}_{0.5}\text{O}_3$ (d).

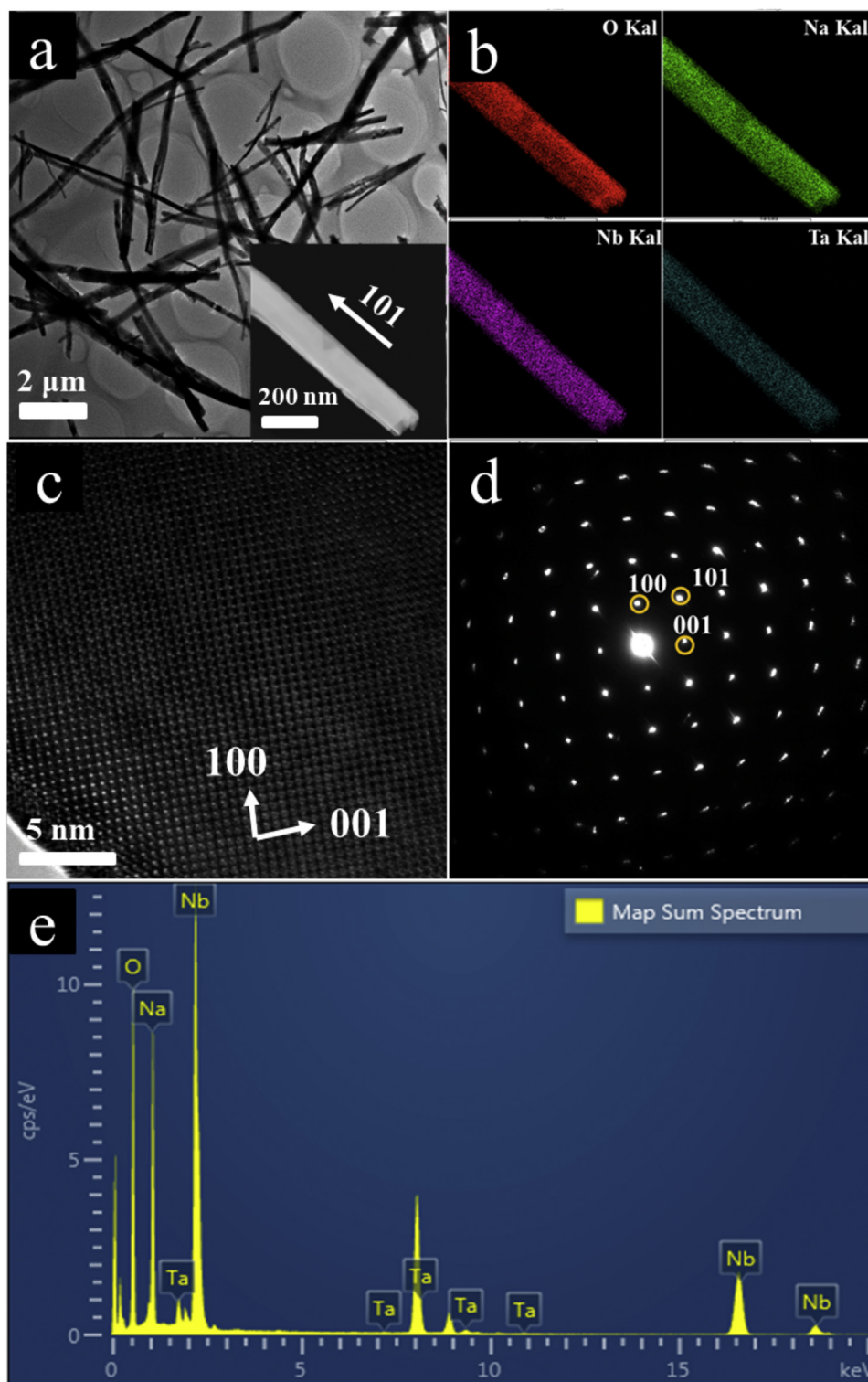


Fig. 3. TEM image of $\text{NaNb}_{0.875}\text{Ta}_{0.125}\text{O}_3$ (a) and the corresponding elemental mapping results (b); the HRTEM image (c), SAED (d) and EDS pattern (e) of $\text{NaNb}_{0.875}\text{Ta}_{0.125}\text{O}_3$.

by contrast with NaNbO_3 , quite distinction of NaTaO_3 was synthesized at the same condition. As observed in Fig. S1(b), the NaTaO_3 has an aggregated nanoparticles shape with diameters of 50–200 nm. A comparison of $\text{NaNb}_{1-x}\text{Ta}_x\text{O}_3$ was displayed in Fig. 2. As shown, the samples present the same 1D wire-like structures with NaNbO_3 when Nb:Ta ratio is more than or equal to 7:1 (Fig. 2(a) and (b)), indicating tantalum successfully penetrates into the lattice of NaNbO_3 . However, few nanoparticles emerge

and uniformly distribute on the surface of wire when extending Nb/Ta ratio to 3:1 (Fig. 2(c)). Upon further improving Ta content, more nanoparticles will coat and even agglomerate on the surface or interspace of wire (Fig. 2(d)), suggesting the independent perovskite-type NaTaO_3 nanoparticles are formed at this condition. Therefore, it can be found that precisely controlling the content of Nb/Ta ratio is significantly important to obtain 1D wire-like $\text{NaNb}_{1-x}\text{Ta}_x\text{O}_3$.

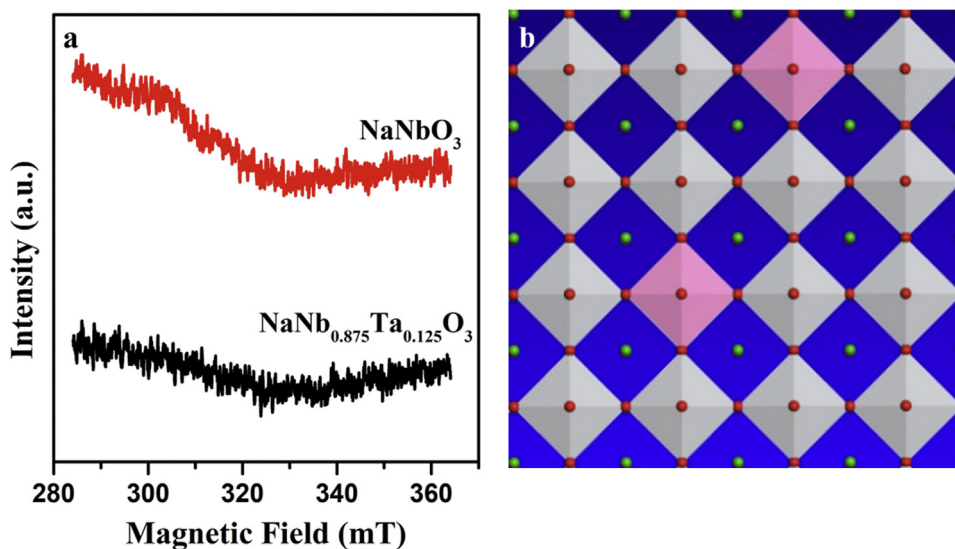


Fig. 4. EPR spectrum at 103 K (a) and crystal structure of $\text{NaNb}_{0.875}\text{Ta}_{0.125}\text{O}_3$ (\blacklozenge NbO_6 unit, \blacklozenge TaO_6 unit) (b).

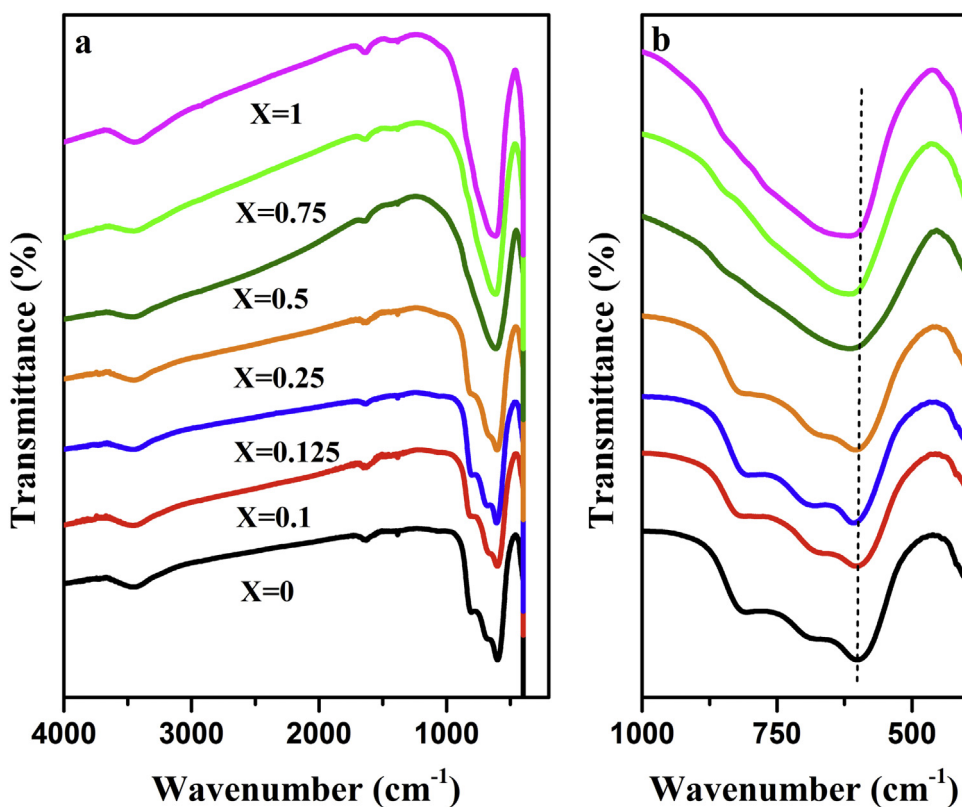


Fig. 5. FT-IR spectra of $\text{NaNb}_{1-x}\text{Ta}_x\text{O}_3$ samples: (a) the survey spectra; (b) the spectra of certain angle.

Moreover, the TEM image of $\text{NaNb}_{0.875}\text{Ta}_{0.125}\text{O}_3$ (Fig. 3(a)) further confirmed its 1D wire-like structure with a typical diameter of ~ 200 nm, which was coincidence with the results of SEM images (Fig. 2(a) and (b)). Energy dispersive X-ray (EDX) elemental mapping images of $\text{NaNb}_{0.875}\text{Ta}_{0.125}\text{O}_3$ show the existence of Na, Nb, Ta and O elements and no other impurity can be detected, as also evidenced by EDS elemental scanning (Fig. 3(b) and (e)). Meanwhile, all of the elements are homogeneously dispersed, again confirming the incorporation of Ta into the lattice of NaNbO_3 . On the other hand, the quite clear and orderly lattice fringes in HRTEM images (Fig. 3(c)) show its supe-

rior crystallinity. It is common acknowledged that higher crystal quality of a sample will dramatically decrease the amount of defects which usually serve as recombination sites. Thus, better crystal quality is favorable for the transport of photo-produced electrons [37]. What's more, a typical selected area electron diffraction (SAED) pattern (Fig. 3(d)) exhibits that $\text{NaNb}_{0.875}\text{Ta}_{0.125}\text{O}_3$ wires have a single-crystalline character, where the wire direction is determined to be along the [101] axis. Therefore, all of these results clearly indicated a small amount of Ta^{5+} successfully substituted the Nb^{5+} sites in NaNbO_3 but still presented its 1D wire-like structure and single-crystalline character when

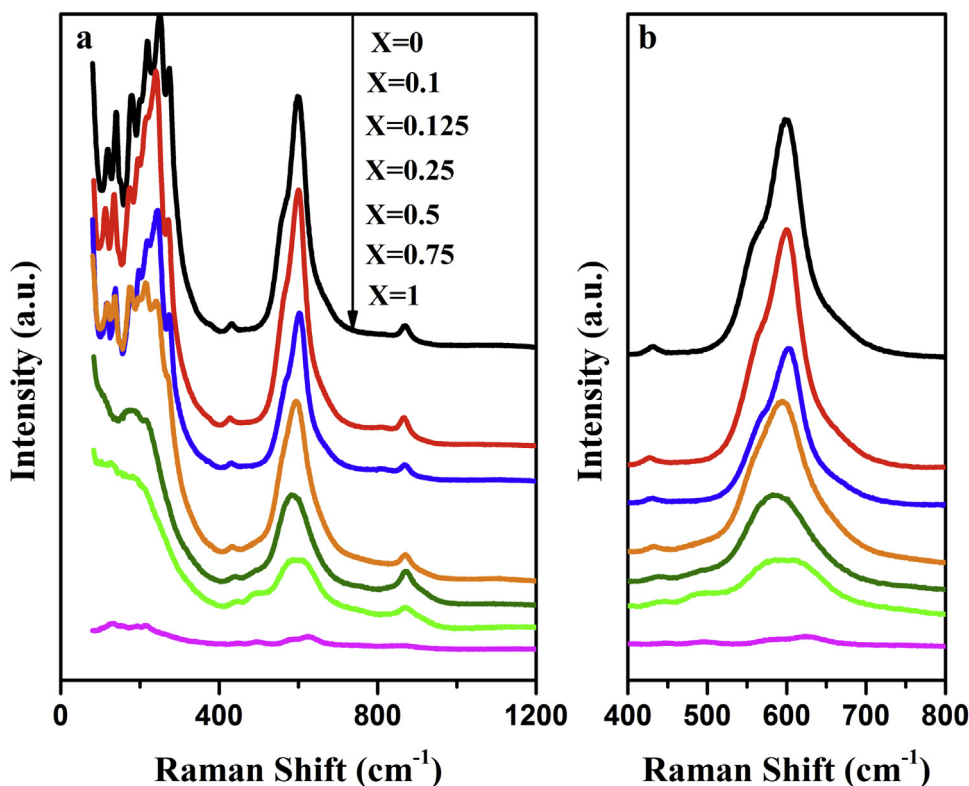


Fig. 6. Raman spectra of $\text{NaNb}_{1-x}\text{Ta}_x\text{O}_3$ samples: (a) the survey spectra; (b) the spectra of certain angle.

Nb/Ta ratio was 7:1. The results were consistent with XRD and SEM.

On the other hand, the concentration of defects of $\text{NaNb}_{0.875}\text{Ta}_{0.125}\text{O}_3$ and NaNbO_3 was explored by low-temperature EPR. Generally, the ESR peak height matches well with the relative content of paramagnetic species. As shown in Fig. 4(a), no signal peaks were observed in the spectra of both NaNbO_3 and $\text{NaNb}_{0.875}\text{Ta}_{0.125}\text{O}_3$ wires, which obviously indicated Ta doping would not produce any defects in the samples. Meanwhile, the O 1s spectra of pure NaNbO_3 and $\text{NaNb}_{0.875}\text{Ta}_{0.125}\text{O}_3$ wires are shown in Fig. S2. As can be seen, the O 1s spectra can be deconvoluted into three peaks: lattice oxygen (O_L) at lower binding energy (~ 529.3 eV); weakly bonded oxygen species or/and chemisorbed oxygen (O_C) (~ 531.2 eV) and surface oxygen (O_S) at the highest binding energy (~ 533.4 eV) [38,39]. The calculated ratios of O_L to O_T ($\text{O}_T = \text{O}_L + \text{O}_C + \text{O}_S$) for NaNbO_3 and $\text{NaNb}_{0.875}\text{Ta}_{0.125}\text{O}_3$ were 75.0 % and 77.5 %, respectively. Obviously, the lattice oxygen (O_L) changed very little after incorporation of Ta. The result indicated Ta-incorporation introduces no defects in the wires, which is well consistent with low-temperature EPR. Based on the experiments discussed above, a possible crystal structure of $\text{NaNb}_{0.875}\text{Ta}_{0.125}\text{O}_3$ wires was elucidated in Fig. 4(b). Unlike the perovskite structure of NaNbO_3 , $\text{NaNb}_{0.875}\text{Ta}_{0.125}\text{O}_3$ consists of NbO_6 and TaO_6 octahedral with Na ions occupy sites in channels of octahedral structure. The introduction of Ta will partial substitute the Nb sites of NaNbO_3 , which has been demonstrated by XRD and HRTEM. Moreover, the addition of Ta will not only maintain the wire-like morphology of NaNbO_3 , but also present a long-range ordered single-crystalline structure, which is favorable for a photocatalytic reaction.

FT-IR and Raman spectra were used to investigate the effect of Ta doping on the crystal structure of NaNbO_3 . According to the results in Fig. 5(a), all samples exhibit peaks at 1650 and 3000–3500 cm^{-1} , corresponding to the vibrations of O–H and H–O–

H. Meanwhile, the sharp bands below 1000 cm^{-1} are assigned to the stretching model of the Na-niobate octahedral framework including Nb–O stretching, Nb–O–Nb bending and lattice vibrations [34]. With the increase of Ta amount, the characteristic absorption peaks below 1000 cm^{-1} slightly shift to higher wavenumber and are eventually replaced by a broad peaks (Fig. 5(b)), indicating the doping of Ta results in the distortion of $[\text{NbO}_6]$ octahedral structure.

Meanwhile, the Raman spectra of pure NaNbO_3 are well consistent with the previous report [40,41], in which the band around 600 cm^{-1} is attributed to the typical stretching model of Nb–O octahedron (Fig. 6). By contrast with different proportions of $\text{NaNb}_{1-x}\text{Ta}_x\text{O}_3$, the intensity of the characteristic peaks below 300 cm^{-1} gradually decrease and almost disappear with the increase of Nb/Ta ratio (Fig. 6(a)). Moreover, the characteristic peak at 600 cm^{-1} moves to the direction of lower wave number, further indicating the distortion related to the rotation of octahedron caused by the incorporation of Ta into NaNbO_3 (Fig. 6(b)) [42].

Thus, according to the results discussed above, although Nb^{5+} has almost identical radius to Ta^{5+} , the atomic weight of Nb^{5+} is smaller than that of Ta^{5+} . The changing of stretching vibration frequencies were possibly caused by the disparate atomic weights between Nb^{5+} and Ta^{5+} . According to the literature report, lattice vibration has a significant impact on the charge transport inside the semiconductor, which directly determines the charge separation efficiency of a photocatalyst [43]. Moreover, the efficient charge separation of a photocatalyst greatly determines its photocatalytic performance. Thus, the Ta doping will probably make a positive effect on the photo-activity of NaNbO_3 .

XPS spectra were applied to study the chemical state of $\text{NaNb}_{1-x}\text{Ta}_x\text{O}_3$. Firstly, the survey spectra in Fig. 7(a) illustrate the coexistence of Na, Nb, Ta and O elements as expected. However, the signal of Ta can be only detected when Nb/Ta ratio is less than

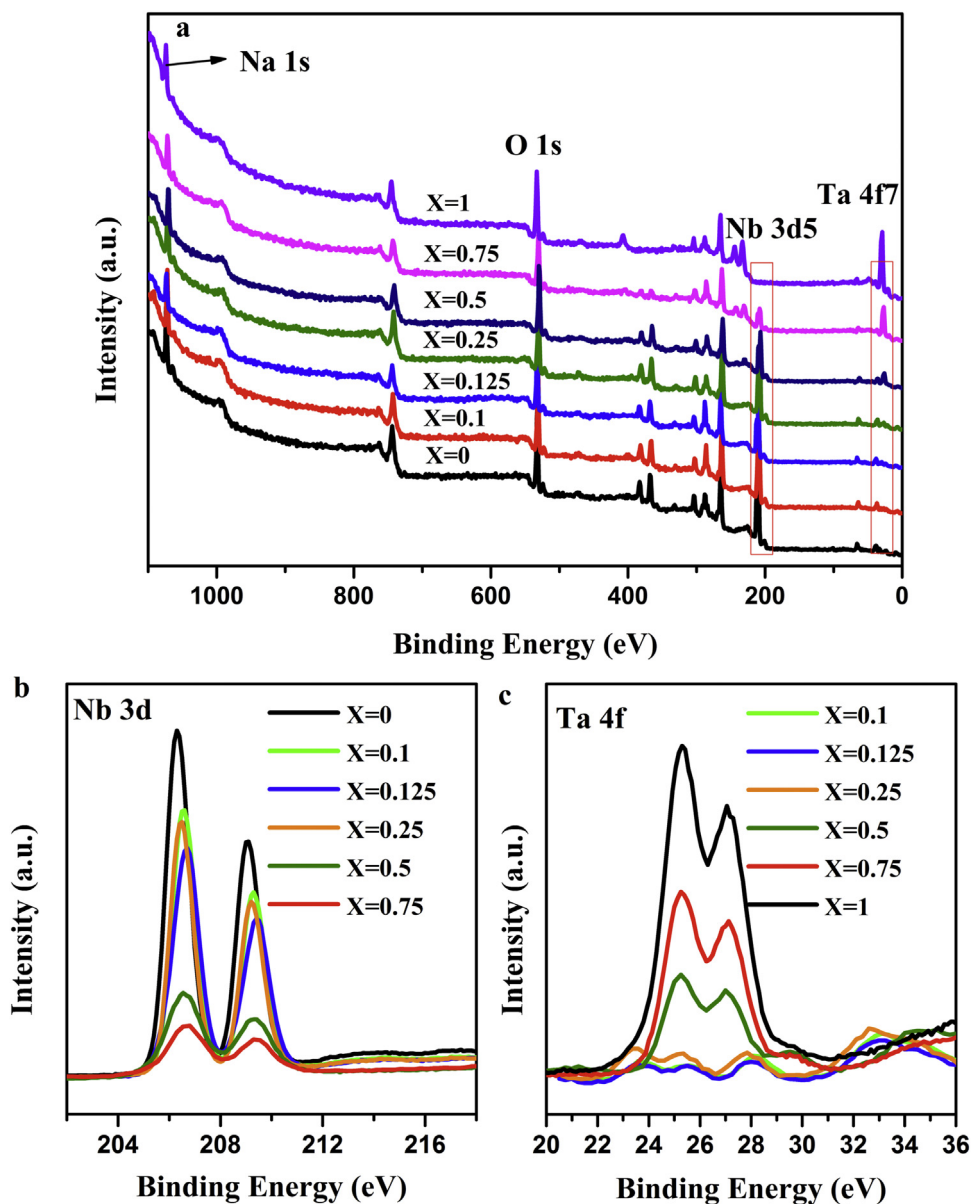


Fig. 7. The survey XPS spectra of $\text{NaNb}_{1-x}\text{Ta}_x\text{O}_3$ (a) and the XPS spectra of $\text{NaNb}_{1-x}\text{Ta}_x\text{O}_3$ in the Nb 3d (b) and Ta 4f (c) regions.

7:1 and its intensity increases gradually along with increasing Ta amount. Meanwhile, the Nb 3d spectrum of NaNbO_3 show two peaks at 206.3 eV (Nb 3d_{5/2}) and 209.1 eV (Nb 3d_{3/2}), which are attributed to Nb⁵⁺ chemical state. By contrast with bare NaNbO_3 , the Nb 3d peaks of $\text{NaNb}_{1-x}\text{Ta}_x\text{O}_3$ shift to the direction of higher binding energy, which is possibly ascribed to the substitution of Ta for Nb (Fig. 7(b)). On the other hand, the Ta 4f spectrum of pure NaNbO_3 can be split into two peaks at 25.3 eV (Nb 3d_{7/2}) and 27.1 eV (Nb 3d_{5/2}), indicating Ta is in the Ta (5+) chemical state. Moreover, almost no Ta 4f peaks were observed when the proportion of Nb to Ta is higher than 3:1 (Fig. 7(c)). As we all know, XPS is a surface analysis technology, which always measures the surface content of materials. Given the above phenomenon, it can be inferred that almost all of tantalum successfully enter into the lattice of NaNbO_3 when Nb/Ta ratio is greater than 3:1. While, with further increasing of Ta content, some of Ta (in the form of NaNbO_3) will emerge on the surface of NaNbO_3 , corresponding to the increasing intensity of Ta 4f spectrum. This conclusion is coincidence with the results of XRD and SEM&TEM.

3.2. Optical properties

The photoabsorption ability of $\text{NaNb}_{1-x}\text{Ta}_x\text{O}_3$ were probed by UV-vis DRS. As depicted in Fig. 8(a), all samples have an absorption edge between 380 and 400 nm. Moreover, the absorption edges gradually move to higher wavelength with extending Nb content, suggesting there is an optical capacity increment by contrast with bare NaNbO_3 . The band gap energies (E_g) of samples can be calculated through the Kubelka-Munk equation [44–46]: $ah\nu = A(h\nu - E_g)^{n/2}$ ($n = 4$ for NaNbO_3 and $n = 1$ for NaNbO_3). Based on the plot of $(ah\nu)^{1/2}$ and $(ah\nu)^2$ vs. $(h\nu)$ in Fig. 8(b) and (c) and Fig. S3, the band gaps of $\text{NaNb}_{1-x}\text{Ta}_x\text{O}_3$ (from $x = 0$ to $x = 1$) are calculated to be 2.99, 3.37, 3.39, 3.40, 3.36, 3.44 eV and 3.70 eV, respectively. Generally, the valence and conduction band of a transition metal oxide always consists of O 2p and transition metal d orbitals [47]. Therefore, all valence top values of the as-prepared samples should be similar because the valence bands consist of only O 2p orbitals and the O²⁻ coordinate to Nb⁵⁺ or Ta⁵⁺ with the same ionic radius. From the valence band (VB) XPS spectra, the EVB of the samples can

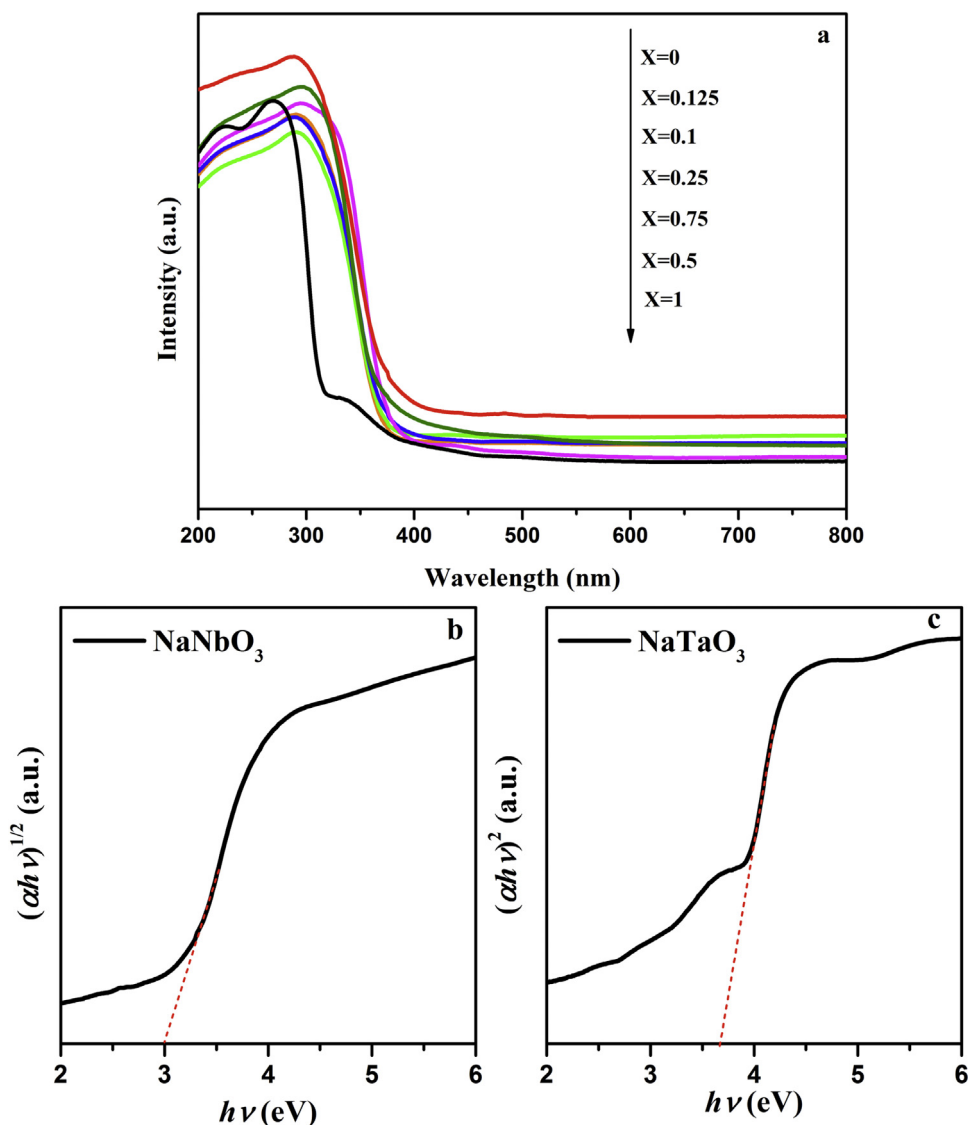


Fig. 8. UV-vis diffuse-reflectance spectra of different $\text{NaNb}_{1-x}\text{Ta}_x\text{O}_3$ photocatalysts (a) and the plot of $(\alpha h\nu)^n$ vs. photon energy ($h\nu$) of NaNbO_3 (b), NaTaO_3 (c).

be ascribed to 1.85 eV (Fig. S4). Thus, according to the results of the UV-vis diffuse reflectance spectra and VB-XPS, the band structures of the prepared samples were illustrated in Fig. S5. Clearly, after incorporation with Ta, the conduction potential of $\text{Na}(\text{Nb,Ta})\text{O}_3$ is more negative than NaNbO_3 [48,49]. This is beneficial to increase the driving force of electrons during the process of reducing water and promote the transfer of photogenerated electrons. However, the large band gap is undesirable for the light absorption of a photocatalyst. Therefore, a balance between the reduction power and the light absorption ability is greatly important to improve the photocatalytic performance of $\text{NaNb}_{1-x}\text{Ta}_x\text{O}_3$.

3.3. Photocatalytic tests

The photocatalytic H_2 evolution of $\text{NaNb}_{1-x}\text{Ta}_x\text{O}_3$ photocatalysts was evaluated under mimic sunlight irradiation. As depicted in Fig. 9, a H_2 evolution rate of $302.1 \mu\text{mol g}^{-1} \text{h}^{-1}$ was achieved on pure NaNbO_3 wires, appropriately 23 folds higher than that of NaTaO_3 nanoparticles ($12.9 \mu\text{mol g}^{-1} \text{h}^{-1}$) (Fig. 9(c) and Table S2). These results are possibly ascribed to the great distinction of morphology and band gap between NaNbO_3 and NaTaO_3 . In addition, by comparison with NaTaO_3 , the photocatalytic performance

of $\text{Na}(\text{Nb,Ta})\text{O}_3$ was significantly enhanced with increasing Nb amount. Especially, higher H_2 -production efficiency than NaNbO_3 was achieved when Nb/Ta ratio was not lower than 3 (Fig. 9(a) and (b)). According to the results of XRD, the products still have the same perovskite-type structures as NaNbO_3 when Nb/Ta ratio is 3:1 or higher. The introduction of Ta will increase the redox ability of electrons and also lead to a distorted octahedral structure compared with NaNbO_3 (confirmed by UV-vis DRS, FT-IR and Raman spectra). These results will significantly promote the migration of photo-generated electrons, which in turn enhance the photocatalytic efficiency when Nb/Ta ratio is 3:1 or more (Fig. 9(a) and (b)). In addition, the $\text{NaNb}_{0.875}\text{Ta}_{0.125}\text{O}_3$ exhibits the optimal H_2 evolution rate ($523.5 \mu\text{mol g}^{-1} \text{h}^{-1}$) among all of samples, which is appropriately 41 and 2 folds higher than that of bare NaTaO_3 and NaNbO_3 (Fig. 9(c) and Table S1). From the results of SEM&TEM, the single crystalline wire-like morphology could be successfully maintained when the ratio was 7:1. It is well known that the perfect 1D wires possess abundant active sites in their linear morphology, which is conducive to a photoreaction. However, nanoparticles will cover on the surface of wires with excessive Ta amount, which will reduce the active sites. Therefore, the synergistic effect of appropriate content for Ta-substituted Nb and the maintaining of wire-like

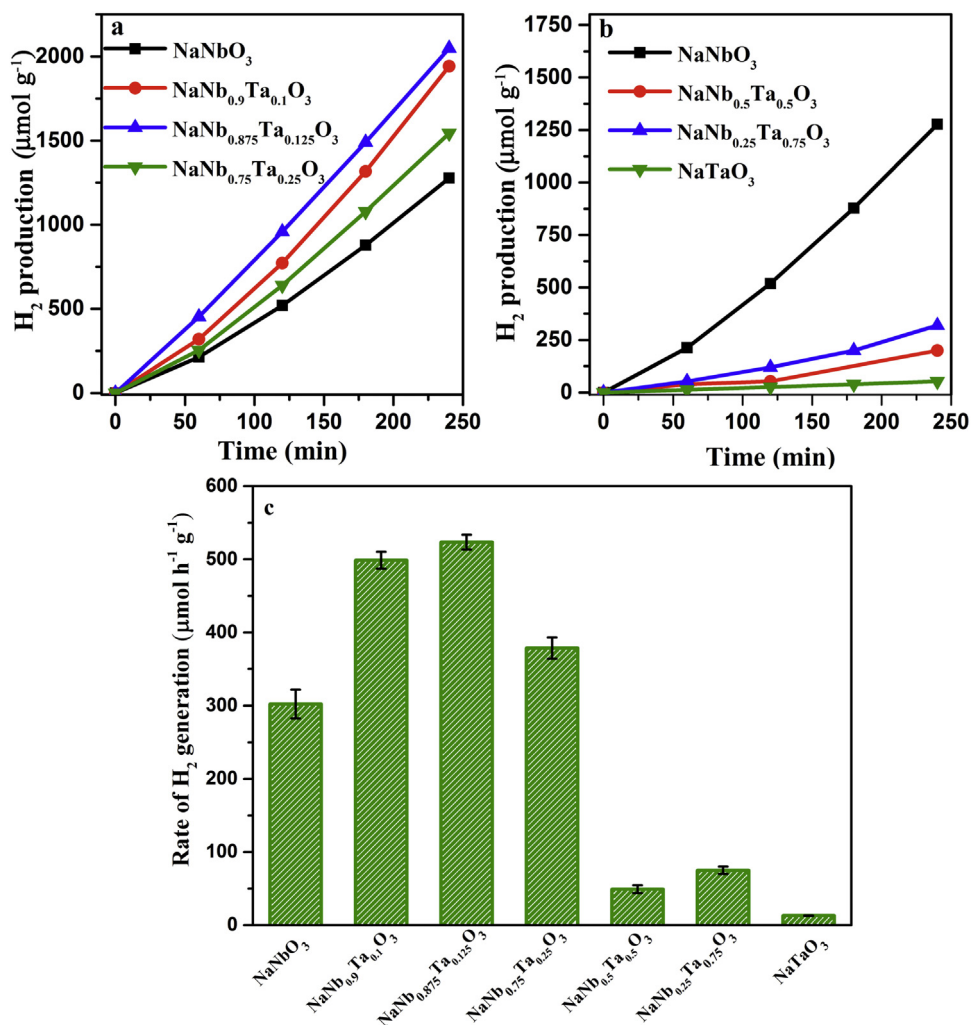


Fig. 9. Photocatalytic H₂ production under sunlight irradiation (a, b) and the H₂ production rates of various photocatalysts (error bars represent the standard deviation for three parallel experiments) (c).

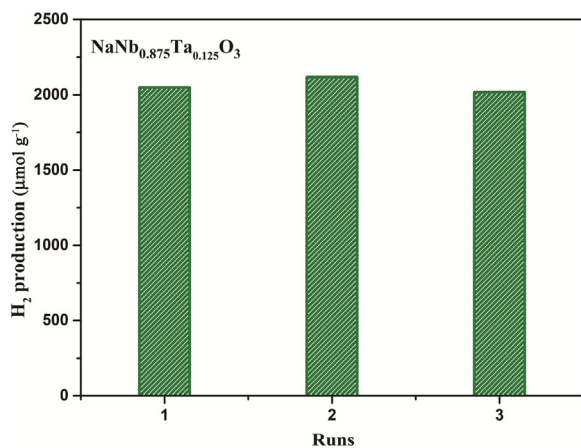


Fig. 10. Recyclability of NaNb_{0.875}Ta_{0.125}O₃ for the photocatalytic H₂ production.

morphology together resulted in the highest photocatalytic activity of NaNb_{0.875}Ta_{0.125}O₃.

Additionally, the stability and reusability of NaNb_{0.875}Ta_{0.125}O₃ has been explored because it is vital to practical application. As illustrated in Fig. 10, the amount of H₂ still remained at 504.5 μmol g⁻¹ h⁻¹ after three repeated cycles, exceeding 90 % of the original

activity. Therefore, it can be inferred that NaNb_{0.875}Ta_{0.125}O₃ is sufficiently stable during the course of photocatalytic H₂ production.

3.4. Possible photocatalytic mechanism

Since the fast interfacial charge transfer is one of important factors for photocatalytic property [50], the PL spectra were firstly evaluated at excitation wavelengths of 280 nm. As displayed in Fig. 11(a), the intensity of NaNb_{0.875}Ta_{0.125}O₃ is slightly lower than that of pristine NaNbO₃, which demonstrates a higher efficiency of charge separation towards NaNb_{0.875}Ta_{0.125}O₃ [51]. This point is further identified by the transient photocurrent responses. Generally, a higher intensity of photocurrent corresponds to a better separation efficiency of photogenerated e–h pairs. As exhibited in Fig. 11(b), the peak intensity of NaNb_{0.875}Ta_{0.125}O₃ is prominently higher than that of NaNbO₃, further confirming the doping of Ta significantly reduces the recombination of photogenerated e–h pairs. Besides, from EIS spectra (Fig. 11(c)), NaNb_{0.875}Ta_{0.125}O₃ exhibits significantly smaller radius than that of NaNbO₃, confirming a faster interfacial charge transfer property. Moreover, as shown in Fig. 11(d), NaNb_{0.875}Ta_{0.125}O₃ has a longer lifetime, corresponding to a slower charge recombination of the excited state. Through fitting the decay spectra, the average fluorescence lifetimes of NaNb_{0.875}Ta_{0.125}O₃ and NaNbO₃ were estimated to be 1.54 ns and 2.40 ns. The longer photocarriers lifetime of NaNb_{0.875}Ta_{0.125}O₃

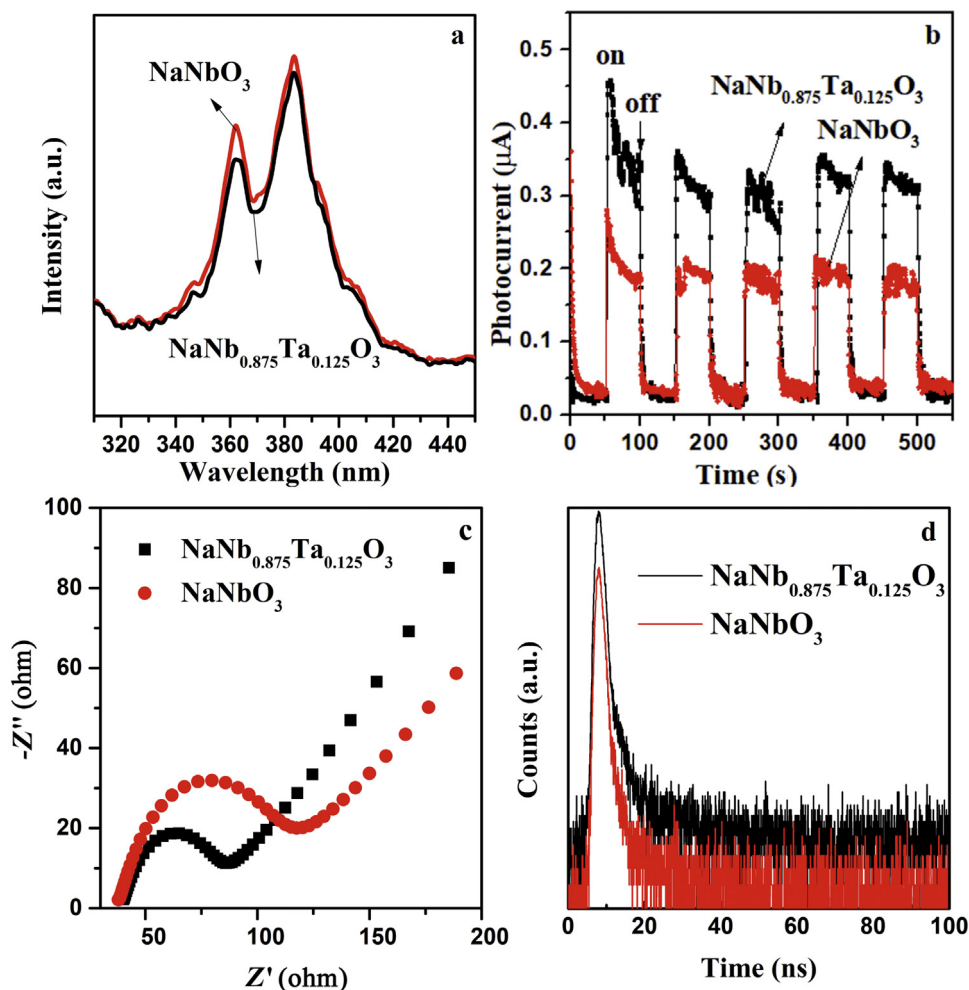
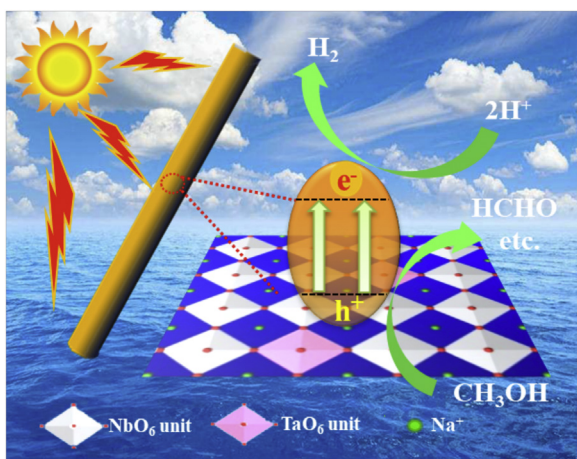


Fig. 11. Emission photoluminescence (PL) spectra (a), photocurrent (b), electrochemical impedance spectra (c) and time-resolved PL decay curves (d) of pure NaNbO_3 and $\text{NaNb}_{0.875}\text{Ta}_{0.125}\text{O}_3$.



Scheme 1. Schematic illustration of the mechanism of $\text{NaNb}_{0.875}\text{Ta}_{0.125}\text{O}_3$ during photocatalytic H_2 production.

maximized the utilization of photoenergy, so as to enhance the photocatalytic activity [52–54].

On the basis of the above analyses, a possible mechanism of $\text{NaNb}_{0.875}\text{Ta}_{0.125}\text{O}_3$ was presented and illustrated in Scheme 1. As the CB edge potential is more negative than that of H_2 , the photo-generated electrons will be transfer quickly to the CB edge

of $\text{NaNb}_{0.875}\text{Ta}_{0.125}\text{O}_3$ to reduce protons to hydrogen, suppressing the recombination of e^-h^+ pairs. While, the photo-generated holes in the VB of $\text{NaNb}_{0.875}\text{Ta}_{0.125}\text{O}_3$ will react with methanol (sacrificial reagent) to prolong the lifetime of charge carries. The improved photocatalytic performances of $\text{NaNb}_{0.875}\text{Ta}_{0.125}\text{O}_3$ wires are mainly ascribed to the following factors: (i) Wires with perfect 1D morphology (confirmed by SEM&TEM) can generate more active sites and have easier accessibility to the active sites; (ii) Single-crystalline character dramatically reduces the amount of defects, which greatly facilitates the transfer of electrons; (iii) The more negative conduction potential makes a stronger reduction power for the H_2 evolution; (iv) The structural distortions caused by the partial Ta-substituted Nb will improve the separation efficiency of charge carriers.

4. Conclusion

In summary, we manage to fabricate single-crystalline $\text{NaNb}_{0.875}\text{Ta}_{0.125}\text{O}_3$ wires through a simple hydrothermal method. The results indicated that doping of Ta into the matrix of NaNbO_3 would make a dramatically difference in the morphology, band gap structure and separation efficiency of charge carriers of the samples, which remarkably influenced their photocatalytic performance. What's more, by contrast with pure NaNbO_3 and NaTaO_3 , a significantly improved photocatalytic H_2 evolution of $\text{NaNb}_{0.875}\text{Ta}_{0.125}\text{O}_3$ was obtained, which also presented superior

stability. The improved activity was mainly ascribed to its synergistic effect between appropriate Ta doping and perfect 1D wire-like morphology, which resulted in fewer defects, larger reduction capability of electrons and higher separation capability of electron-hole pairs. This work provides new insights into understanding the mechanism of photocatalytic performances and offers a promising multi-component material for H₂ evolution and storage.

Acknowledgements

This work was financially supported by the Natural Science Foundation of Shanghai (No. 19ZR1403500), the National Natural Science Foundation of China (Nos. 21373054, 21773291 and 61904118), the Natural Science Foundation of Jiangsu (Nos. BK20190935 and BK20190947), the Natural Science Foundation of the Jiangsu Higher Education Institutions of China (Nos. 19KJJA210005, 19KJB510012, 19KJB120005 and 19KJB430034), the Suzhou Key Laboratory for Nanophotonic and Nanoelectronic Materials and its Devices (No. SZS201812) and Jiangsu Key Laboratory for Environment Functional Materials.

Appendix A. Supplementary data

Supplementary material related to this article can be found, in the online version, at doi:<https://doi.org/10.1016/j.jmst.2020.05.006>.

References

- [1] Q. Li, H. Meng, P. Zhou, Y. Zheng, J. Wang, J. Yu, J. Gong, *ACS Catal.* 3 (2013) 882–889.
- [2] J.G. Yu, J.R. Ran, *Energy Environ. Sci.* 4 (2011) 1364–1371.
- [3] Q.J. Xiang, J.G. Yu, *J. Phys. Chem. Lett.* 4 (2013) 753–759.
- [4] L. Jiang, X. Yuan, G. Zeng, J. Liang, Z. Wu, H. Wang, *Environ. Sci. Nano* 5 (2018) 599–615.
- [5] C. Chen, Y. Zhao, S. Lu, K. Li, Y. Li, B. Yang, F. Yi, *Adv. Energy Mater.* 7 (2017), 1700866.
- [6] C.Y. Lee, A.C. Taylor, S. Beirne, G.G. Wallace, *Adv. Energy Mater.* 7 (2017), 1701060.
- [7] C. Gao, T. Wei, Y. Zhang, X. Song, Y. Huan, H. Liu, M. Zhao, J. Yu, X. Chen, *Adv. Mater.* 31 (2019), 1806596.
- [8] Y. Yu, W. Yan, X. Wang, P. Li, W. Gao, H. Zou, K. Ding, *Adv. Mater.* 30 (2018), 1705060.
- [9] J. Ran, W. Guo, H. Wang, B. Zhu, J. Yu, S.Z. Qiao, *Adv. Mater.* 30 (2018), 1800128.
- [10] N. Tian, Y. Zhang, X. Li, K. Xiao, X. Du, F. Dong, G.I.N. Waterhouse, T. Zhang, H. Huang, *Nano Energy* 38 (2017) 72–81.
- [11] T. Arai, S. Senda, Y. Sato, H. Takahashi, K. Shinoda, B. Jeyadevan, K. Tohji, *Chem. Mater.* 20 (2008) 1997–2000.
- [12] L. Zheng, S. Han, H. Liu, P. Yu, X. Fang, *Small* 12 (2016) 1527–1536.
- [13] L. Lin, W. Ren, C. Wang, A. Asiri, M.J. Zhang, X. Wang, *Appl. Catal. B: Environ.* 231 (2018) 234–241.
- [14] C. Wang, M. Zhang, X. Chen, M. Bertrand, A. Shams-Ansari, S. Chandrasekhar, P. Winzer, M. Lončar, *Nature* 562 (2018) 101–104.
- [15] Q. Liu, Y. Chai, L. Zhang, J. Ren, W.L. Dai, *Appl. Catal. B: Environ.* 205 (2017) 505–513.
- [16] Y. Su, Y. Zhao, Y. Zhao, J. Lang, X. Xin, X. Wang, *Appl. Surf. Sci.* 358 (2015) 213–222.
- [17] S. Liang, R. Liang, L. Wen, R. Yuan, L. Wu, X. Fu, *Appl. Catal. B: Environ.* 125 (2012) 103–110.
- [18] J.N. Kondo, M. Uchida, K. Nakajima, L. Daling, M. Hara, K. Domen, *Chem. Mater.* 16 (2004) 4304–4310.
- [19] J.M. Wu, I. Djerdj, T. von Graberg, B.M. Smarsly, *Beilstein J. Nanotech.* 3 (2012) 123–133.
- [20] Q.Q. Liu, L. Zhang, Y.Y. Chai, W.L. Dai, *J. Phys. Chem. C* 121 (2017) 25898–25907.
- [21] H. Fujito, H. Kunioku, D. Kato, H. Suzuki, M. Higashi, H. Kageyama, R. Abe, *J. Am. Chem. Soc.* 138 (2016) 2082–2085.
- [22] D.B. Xu, S.B. Yang, Y. Jin, M. Chen, W.Q. Fan, B.F. Luo, W.D. Shi, *Langmuir* 31 (2015) 9694–9699.
- [23] W. Wang, M.O. Tadé, Z. Shao, *Chem. Soc. Rev.* 44 (2015) 5371–5408.
- [24] O. Palasyuk, P.A. Maggard, *J. Solid State Chem.* 191 (2012) 263–270.
- [25] K.I. Shimizu, Y. Tsuji, T. Hatamachi, K. Toda, T. Kodama, M. Sato, Y. Kitayama, *Phys. Chem. Chem. Phys.* 6 (2004) 1064–1069.
- [26] E. Garcia-Gonzalez, A. Torres-Pardo, R. Jimenez, J.M. Gonzalez-Calbet, *Chem. Mater.* 19 (2007) 3575–3580.
- [27] M. Prades, N. Masó, H. Beltrán, E. Cordoncillo, A.R. West, *Inorg. Chem.* 52 (2013) 1729–1736.
- [28] P. Jana, A. Victor, C.M. Montero, P. Gálvez, P. Pizarro, J.M. Coronado, D.P. Serrano, *Green Chem.* 17 (2015) 1735–1743.
- [29] S.S.K. Ma, T. Hisatomi, K. Maeda, Y. Moriya, K. Domen, *J. Am. Chem. Soc.* 134 (2012) 19993–19996.
- [30] D. Zhang, J. Cheng, F. Shi, Z. Cheng, X. Yang, M. Cao, *RSC Adv.* 5 (2015) 33001–33007.
- [31] X. Jiang, T. Wang, *Environ. Sci. Technol.* 41 (2007) 4441–4446.
- [32] Y. Wang, Z. Zhang, Y. Zhu, Z. Li, R. Vajtai, L. Ci, P.M. Ajayan, *ACS Nano* 2 (2008) 1492–1496.
- [33] Q.L. Gu, K.J. Zhu, N.S. Zhang, Q.M. Sun, P.C. Liu, J.S. Liu, J. Wang, Z.S. Li, *J. Phys. Chem. C* 119 (2015) 25956–25964.
- [34] A. Yu, J. Qian, L. Liu, H. Pan, X. Zhou, *Appl. Surf. Sci.* 258 (2012) 3490–3496.
- [35] D.R. Liu, Y.S. Jiang, G.M. Gao, *Chemosphere* 83 (2011) 1546–1552.
- [36] R.D. Shannon, *Acta Cryst. A* 32 (1976) 751–767.
- [37] S. Zhu, S. Liang, J. Bi, M. Liu, L. Zhou, L. Wu, X. Wang, *Green Chem.* 18 (2016) 1355–1363.
- [38] J. Yu, Z. Si, L. Chen, X. Wu, D. Weng, *Appl. Catal. B: Environ.* 163 (2015) 223–232.
- [39] Y. Wang, F. Wang, Y. Chen, D. Zhang, B. Li, S. Kang, X. Li, L. Cui, *Appl. Catal. B: Environ.* 147 (2014) 602–609.
- [40] V. Shanker, S.L. Samal, G.K. Pradhan, C. Narayana, A.K. Ganguli, *Solid State Sci.* 11 (2009) 562–569.
- [41] Y. Shiratori, A. Magrez, J. Dornseiffer, F.H. Haegel, C. Pithan, R. Waser, *J. Phys. Chem. B* 109 (2005) 20122–20130.
- [42] K. Maeda, K. Domen, *Angew. Chem. Int. Ed.* 51 (2012) 9865–9869.
- [43] J. Yin, Z. Zou, J. Ye, *J. Phys. Chem. B* 108 (2004) 8888–8893.
- [44] M.A. Butler, *J. Appl. Phys.* 48 (1977) 1914–1920.
- [45] J. Zeng, H. Wang, Y. Zhang, M.K. Zhu, H. Yan, *J. Phys. Chem. C* 111 (2007) 11879–11887.
- [46] Q. Liu, J. Ding, Y. Chai, J. Zhao, S. Cheng, B. Zong, W.L. Dai, *J. Environ. Chem. Eng.* 3 (2015) 1072–1080.
- [47] M. Oshikiriya, M. Boero, J. Ye, Z. Zou, G. Kido, *J. Chem. Phys.* 117 (2002) 7313–7318.
- [48] K. Maeda, *J. Photochem. Photobiol. C: Photochem. Rev.* 12 (2011) 237–268.
- [49] A. Kudo, Y. Miseki, *Chem. Soc. Rev.* 38 (2009) 253–278.
- [50] S. Lin, Y. Zhang, Y. You, C. Zeng, X. Xiao, T. Ma, H. Huang, *Adv. Funct. Mater.* 29 (2019), 1903825.
- [51] W. Li, D. Li, Y. Lin, P. Wang, W. Chen, X. Fu, Y. Shao, *J. Phys. Chem. C* 116 (2012) 3552–3560.
- [52] G.G. Zhang, A. Savateev, Y.B. Zhao, L. Li, M. Antonietti, *J. Mater. Chem. A* 5 (2017) 12723–12728.
- [53] Q. Liu, T.X. Chen, Y.R. Guo, Z.G. Zhang, X.M. Fang, *Appl. Catal. B: Environ.* 193 (2016) 248–258.
- [54] D.S. Yuan, W. Huang, X.R. Chen, Z.Y. Li, J.D.L. Wang, H.W.W.L. Dai, G.F. Guan, *Appl. Surf. Sci.* 489 (2019) 658–667.